Nearshore wave-induced cyclical flexing of sea cliffs

Peter N. Adams
Department of Earth Sciences, University of California, Santa Cruz, California, USA

Curt D. Storlazzi
U.S. Geological Survey, Santa Cruz, California, USA

Robert S. Anderson
Department of Geological Sciences and INSTAAR, University of Colorado, Boulder, Colorado, USA

Received 4 August 2004; revised 21 December 2004; accepted 6 January 2005; published 23 April 2005.

[1] Evolution of a tectonically active coast is driven by geomorphically destructive energy supplied by ocean waves. Wave energy is episodic and concentrated; sea cliffs are battered by the geomorphic wrecking ball every 4–25 s. We measure the response of sea cliffs to wave assault by sensing the ground motion using near-coastal seismometers. Sea cliffs respond to waves in two distinct styles. High-frequency motion (20 Hz) reflects the natural frequency of the sea cliff as it rings in response to direct wave impact. Low-frequency motion in the 0.1–0.05 Hz (10–20 s) band consistently agrees with the dominant nearshore wave period. Integrating microseismic velocities suggests 50 μm and 10 μm displacements in horizontal and vertical directions, respectively. Displacement ellipsoids exhibit simultaneous downward and seaward sea cliff motion with each wave. Video footage corroborates the downward sea cliff flex in response to the imposed water load on the wave cut platform. Gradients in displacement amplitudes documented using multiple seismometers suggest longitudinal and shear strain of the flexing sea cliff on the order of 0.5–4 μ strains during each wave loading cycle. As this sea cliff flexure occurs approximately 3 million times annually, it has the potential to fatigue the rock through cyclical loading. Local sea cliff retreat rates of 10 cm/yr imply that a given parcel of rock is flexed through roughly 10^9 cycles of increasing amplitude before exposure to direct wave attack at the cliff face.

Citation: Adams, P. N., C. D. Storlazzi, and R. S. Anderson (2005), Nearshore wave-induced cyclical flexing of sea cliffs, *J. Geophys. Res.*, *110*, F02002, doi:10.1029/2004JF000217.

1. Introduction

[2] Steep sea cliffs along tectonically active coastal landscapes are the product of wave-induced erosion. Rock uplift delivers fresh rock to the nearshore zone to be attacked by waves delivering their geomorphically effective energy. While one can sense qualitatively the energy of impact by waves crashing against a rocky coast, we have yet to fully understand the processes by which waves impart their energy to the shore and how this energy is transformed into erosion of sea cliffs.

[3] Traditionally, researchers have concluded that waves perform geomorphic work on rocky coasts by mechanical abrasion and by plucking or quarrying of blocks [*Bagnold*, 1939; *Trenhaile*, 1987; *Sunamura*, 1992; *Stephenson and Kirk*, 2000]. Mechanical abrasion employs sediment grains, entrained by wave orbital motions and turbulence, as tools to grind away the face of the sea cliff as the water of sediment-laden breaking waves impacts the vertical surface. Quarrying of blocks is thought to occur by hydraulic action when waves striking the sea cliff compress air in cliff face cracks. This exerts an outward stress on the surrounding rock mass which when repeated causes cracks to grow, ultimately detaching blocks [*Sanders*, 1968]. Importantly, in this view the rate-limiting process is the growth of cracks by wave-induced hydraulic blasts. A major focus of rocky coastline geomorphic research is the documentation of the relative efficacy of each of these processes, and the detailed exploration of the physics of each process.

[4] A new method available to coastal researchers is the use of seismometers to measure directly coastal ground motions incited by waves. Ocean microseisms, first proposed by *Weichert* [1904], are ground motions generated by shallow water waves in coastal regions. They are subdivided into primary and secondary types [*Bormann and Bergman*, 2002]. Primary ocean microseisms involve the conversion of water wave-induced pressure variations to seismic energy, and hence have roughly the same period as the incoming water waves [*Haubrich et al.*, 1963]. Secondary ocean microseisms record pressure variations beneath a standing wave of half the period of the incoming ocean waves. This standing wave exists because the incoming waves are reflected back off the coast, causing superposition

0148-0227/05/2004JF000217$09.00

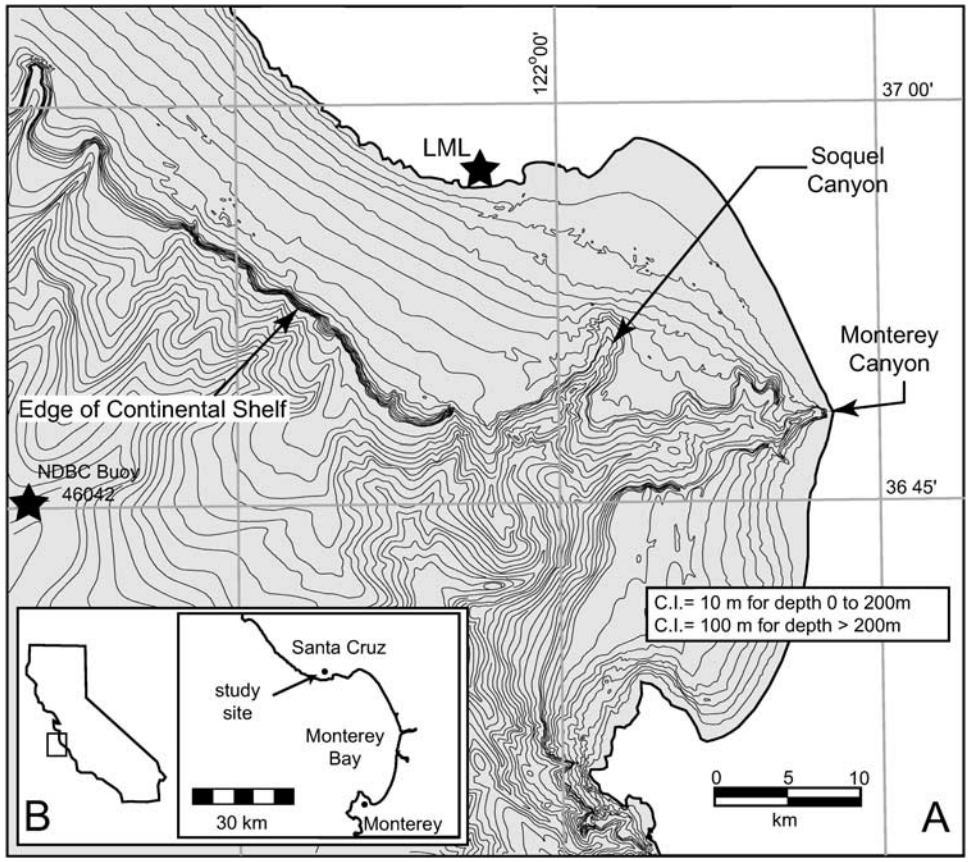

Figure 1. (a) Map of Monterey Bay and (b) its position on the California coast, showing locations of deep water buoy (NDBC Buoy 46042), the onshore microseismic measurement site (Joseph M. Long Marine Lab (LML)), and significant bathymetric features. Note the difference in bathymetric depth contour interval spacing above and below the edge of the continental shelf.

of waves traveling in opposite directions [*Longuet-Higgins*, 1950]. This phenomenon was employed by *Zopf et al.* [1976] to measure ocean waves with a seismometer. The linkage between microseismic energy and wave climate has been explored in detail by *Bromirski and Duennebier* [2002]. Recently, several research groups have hindcast ocean wave climates by examining long-term records of microseismic energy collected at coastal seismic stations [*Tillotson and Komar*, 1997; *Bromirski et al.*, 1999; *Grevemeyer et al.*, 2000; *Bromirski*, 2001].

[5] To understand how changes in offshore wave climate modulate geomorphic energy delivery to a rocky coast, *Adams et al.* [2002] used a broadband seismometer to measure ground motions associated with waves impacting a sea cliff. The purpose of this previous study was to document how offshore wave conditions, shelf bathymetry and tides dictate the temporal pattern of energy delivery to the sea cliffs. Their study focused on the velocity of ground motion, high-pass filtering the data to explore the signal in the frequency band between 1 Hz and the Nyquist frequency (25 Hz) [*Adams et al.*, 2002]. Over the course of that several month-long study, a strong signal in the 0.05–0.1 Hz frequency band (10–20 s period) persisted throughout the time series, but was cautiously ignored, as it was not relevant to the focus on wave-induced, high-frequency shaking. In the study reported here, we revisit this signal explicitly, in a process geomorphology context, asking the questions: (1) How is the long-period (10–20 s, 0.05–0.1 Hz) ground motion signal related to the incident nearshore wave field? (2) What are the details of the motion exhibited by the sea cliff at this frequency? (3) What, if any, strain is the sea cliff experiencing at this frequency?

2. Study Site

[6] The central California coast is etched by numerous embayments, and is decorated with sea cliffs, sea stacks, arches, and pocket beaches [*Griggs and Savoy*, 1985]. Rock uplift along the tectonically active coastal margin and climatically driven sea level oscillations have produced a rugged, rocky, often terraced character of the central California coast. Typically, raised rocky headlands made of erosionally resistant rock protrude seaward and concentrate wave energy through the convergence of wave rays (focusing energy), while sandy beaches are found along recessed portions, where wave rays diverge (diluting energy), spreading energy over a greater length of coast. Our study site is the coastal cliff at the Joseph M. Long Marine Lab (LML) located just northeast of Monterey Bay (Figure 1).

2.1. Regional Setting

[7] Monterey Bay is a crescent-shaped embayment approximately 40 km long, north-south, and 20 km wide, east-west. The shelf is deeply incised by the Monterey and

Soquel Canyons, with shelf width (distance from shore to 120 m bathymetric contour) ranging between 10 and 20 km, with an average offshore slope of between 0.012 and 0.006 (Figure 1). Monterey Bay indents the Salinian tectonic block, bounded by the offshore San Gregorio Fault to the west and the San Andreas Fault to the east [*Greene*, 1977; *Greene and Clark*, 1979; *Ross*, 1979; *Weber*, 1990; *Chin et al.*, 1993]. A flight of five marine terraces immediately north of Monterey Bay testifies that the region has been experiencing uplift during at least five sea level fluctuations. Cosmogenic radionuclide dating of these terraces shows ages corresponding to marine oxygen isotope stages 3, 5a, 5c, 5e, and 7, resulting in a long-term average uplift rate of 1.1 mm/yr [*Perg et al.*, 2001]. Modern sea cliff retreat is highly variable in both time and space around the bay, but long-term (decadal) averaged retreat rates vary from 0 to >30 cm/yr [*Bradley and Griggs*, 1976; *Griggs and Savoy*, 1985; *Hapke and Richmond*, 2002; *Moore and Griggs*, 2002].

2.2. Local Coastal Configuration

[8] The Joseph M. Long Marine Lab property (LML) occupies approximately 0.5 km of cliffed coastline on the northern shore of Monterey Bay (Figure 1a). Sea cliff heights at this site range from 8 to 13 m, and slopes vary from 50° to nearly vertical. High-resolution differential GPS data (gridded portion of Figure 2a) were collected in May 2003 and show the detailed topography of the wave cut platform, sea cliff, and lowest emergent marine terrace. The wave cut platform is exposed at least once daily, as the tidal range varies from approximately 1–2 m over the neap to spring cycle.

2.3. Lithology

[9] The sea cliffs at the LML site are composed of thickly bedded Upper Miocene Santa Cruz Mudstone dipping shallowly (~5°) offshore, capped by a 1–2 m mantle of Quaternary marine terrace sand deposited during the last interglacial [*Dupre*, 1984]. The Santa Cruz Mudstone is mechanically more durable than the stratigraphically higher, less indurated, Purisima Sandstone that crops out further south. Interestingly, the break in lithology between the Santa Cruz and Purisima formations occurs roughly where the coastline changes from convex-seaward to concave-seaward (Figure 1).

2.4. Ocean Wave Climate

[10] The assailing nearshore wave field experienced at LML is a transformed version of the deep water wave climate of offshore central California, which is dominated by either a Northern Hemisphere swell, a Southern Hemisphere swell or local wind-driven seas. From November through March, north Pacific Aleutian cyclones generate a swell that travels toward Monterey Bay, approaching from the northwest (~300°). Depending on the wave period, this swell refracts through a very high angle (up to 80°), losing a significant portion of its deep water wave height and energy per unit length of wave crest before striking the LML site. During the summer months, storms off New Zealand, Indonesia, or Central and South America episodically dispatch a swell of smaller wave height, but longer wave period. This southerly swell approaches from a direction nearly orthogonal to the LML shoreline, losing very little deep water wave height and energy per unit length of wave crest to refraction. Local wind-driven seas dominate when low-pressure systems track near central California. During these times, a poorly organized, short-period westerly to northwesterly swell approaches the LML site [*Meteorology International Inc.*, 1977].

3. Wave/Tide/Microseismic Measurement Methods

[11] We integrate data from four sources in this study. Offshore wave conditions documented by buoys record the unadulterated oceanographic forcing in the system. Nearshore wave conditions documented using pressure gauges reveal the transformed wave after shoaling and refraction over the shallow portion of the continental shelf. The nearshore wave data are valuable because they are representative of the wave conditions actually responsible for delivering destructive geomorphic energy to the system. Tidal data are required to document the location of wave energy deposition, as this is strongly sensitive to water level on a gently sloping (slope ~ 0.01) shelf [*Adams et al.*, 2002]. Microseismic data from portable broadband seismometers measure velocity of ground motion in three directions. These data document sea cliff motion as it responds to assault by waves, which we treat as a proxy for the energy imparted to the sea cliff from the wave field. Each data set is outlined in detail below.

3.1. Offshore Wave Conditions

[12] Hourly offshore wave conditions, including significant wave height, dominant wave period, and mean swell direction are obtained from NOAA's National Data Buoy Center (NDBC) buoy #46042 located approximately 35 km southwest of Santa Cruz, California (Figures 1a and 1b). This device floats on the water surface in a water depth of 1920 m (http://www.ndbc.noaa.gov).

3.2. Nearshore Wave Field

[13] Nearshore wave and tide information are obtained from a NIWA "Dobie-A" wave and tide gauge deployed in ~4 m of water approximately 160 m seaward of the sea cliff edge at the Long Marine Lab study site. This instrument employs a Druck PMP 4000 Series pressure sensor with 0.8 cm accuracy. It collects a 1024 s (~17 min) burst at 2 Hz (2048 points) at the top of every hour to measure waves and tides. Significant wave heights and dominant periods were computed spectrally using a 256 s Hanning-windowed autospectrum with 50% overlap (SuperDUCK method [*Birkemeier et al.*, 1989]), allowing resolution of waves between 3 and 128 s. Dominant wave periods were calculated as the reciprocal of the frequency bearing the greatest quantity of spectral energy. Local tides were computed as the mean water depth over the pressure sensor during each burst.

3.3. Wave Transformation During Shoaling

[14] To illustrate the need for deep water and nearshore wave field measurements, we review the expected wave transformations as waves travel from their source area shoreward. This is covered in detail by *Komar* [1998]. In linear Airy wave theory, waves traveling through water

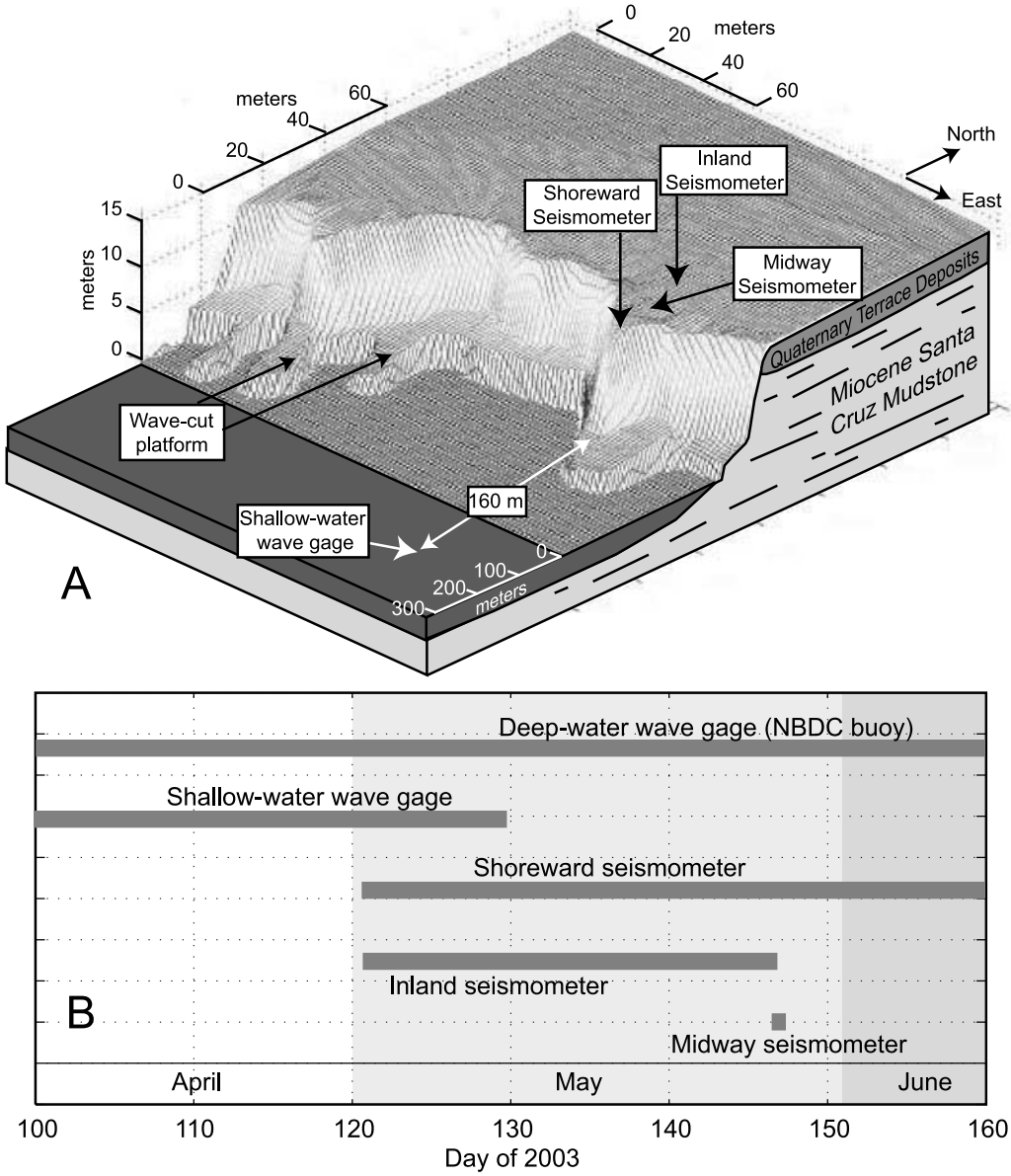

Figure 2. (a) Combination oblique view cartoon and high-resolution GPS data of the LML study site, Santa Cruz, California. Locations of instruments are identified with arrows, and interesting geologic/physiographic components are identified with labels or arrows. GPS data (shown in shaded mesh) were collected during low tide; wave cut platforms appear ~1 m above the sea level surface. Note the difference in horizontal scale between offshore and onshore regions. (b) Timeline showing operational intervals for each instrument used in this study.

depths greater than half their wavelength (the depth extent of wave orbital motion) are considered deep water waves. As waves enter shallow water, their orbital motions interact with the sea floor, causing the wave to slow down. Since wave period is conserved, despite a decrease in wave speed, wavelength is necessarily shortened, and the wave crests become more tightly spaced. Also conserved during shoaling is wave energy flux, a function of wave height and speed, whose decrease is balanced by an increase in energy density. This energy density increase requires an increase in wave height as the wave enters shallow water, providing surfers with a desirable environment. If waves approach the shore obliquely, refraction can change their trajectory and significantly alter the energy density per unit length of wave crest. Wave crests are shortened as refracting waves converge upon a headland, concentrating energy there, whereas wave crests are stretched as refracting waves diverge over an embayment or submarine canyon. This shortening/stretching of wave crests is accompanied by an increase/decrease of shallow water wave height in order to conserve energy.

3.4. Tide Levels

[15] A continuous record of tides is collected by a NOAA tide gauge in Monterey, California. We retrieved these data online and applied a 56 min correction for the Santa Cruz

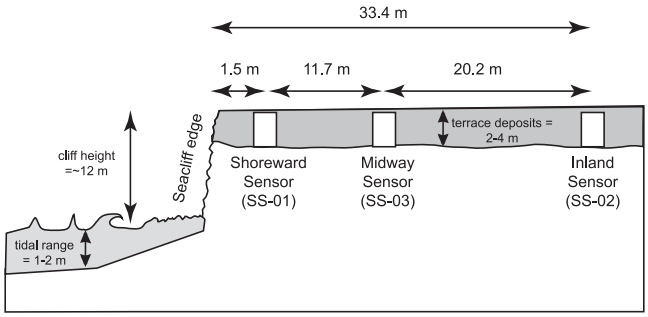

Figure 3. Schematic showing sea cliff height (~12 m), thickness of marine terrace deposits (2–4 m), tidal range (1–2 m), and locations of three seismic stations (SS-01, SS-02, and SS-03) with respect to the sea cliff edge at LML, Santa Cruz, California.

study site as prescribed by the NOAA National Ocean Service Web site (http://tidesandcurrents.noaa.gov). While operational, the nearshore wave and tide gauge collected tidal data that were used to verify the corrected Monterey NOAA data.

3.5. Microseismic Sea Cliff Motion

[16] Two Guralp CMG 40T portable broadband seismometers were deployed at three separate terrace-top seismic stations along a transect perpendicular to the sea cliff edge, shown schematically in Figure 3. These instruments measure velocity for three separate directions of ground motion (vertical, north-south, and east-west). These ground motion velocities can be differentiated to obtain ground accelerations, or integrated to obtain absolute displacements.

[17] Seismic station 1 (SS-01) was located as close to the sea cliff edge as the sensor could be buried (~1.5 m from absolute edge) and was operational from year-day 120–160, (30 April–9 June) of 2003. Seismic Station 2 (SS-02) was placed 30 meters landward of SS-01 on a line perpendicular to the trend of the sea cliff edge, and was operational from year-day 120–146 (30 April–26 May 26). The sensor from SS-02 was moved 18 m shoreward (9 m from the sea cliff edge) on year-day 146 (26 May) in order to occupy a third seismic station (SS-03) for 6 hours spanning year-days 146 and 147 (26–27 May). Locations of the three seismic stations are shown in Figure 2a, while durations of each instrument's operation, showing times of overlapping data acquisition, are given in Figure 2b.

4. Results

[18] Hourly wave conditions over a period of observation are shown in Figure 4. The record from the deep water buoy includes hourly burst averages of significant wave height, dominant period, and swell direction, whereas the record from the nearshore wave gauge includes only hourly burst averages of significant wave height and dominant period. Differences between the deep water and nearshore conditions are examined below.

4.1. Wave Height

[19] Deep water significant wave heights varied between 1 and 5 m whereas nearshore significant wave heights varied between 0.5 and 1.5 m (Figure 4a). During the period of overlapping instrument operation (year-days 100–129), average nearshore significant wave height (H_n = 0.82 m) was approximately 35% of the average deep water significant wave height (H_d = 2.38 m), due to wave transformation during refraction and shoaling. In other words, the majority of the waves approach from angles that induce significant refraction, causing stretching of wave crests and attendant reduction of wave heights prior to impact on the coastline. Frequency distributions indicate the population of nearshore wave heights was more tightly distributed than the population of deep water wave heights due to shoaling and refraction.

4.2. Wave Period

[20] Spectrally dominant wave periods ranged between 5 and 20 s in deep water, and between 5 and 15 s in the nearshore during the observation interval (Figure 4c). Although wave period is conserved, the deep water buoy often witnessed a slightly different wave field than the nearshore wave gauge because some offshore wave groups follow ray paths that miss the nearshore study site entirely. Dominant deep water wave periods have a Poisson-type distribution with a mean of 10.8 s and a standard deviation of ±2.9 s. Dominant nearshore wave periods are normally distributed about a mean of 8.6 s with a standard deviation of ±1.5 s.

4.3. Swell Direction

[21] Dominant swell directions were from north to west during 75% of the observation period and from the south to west during 25% (Figure 4d). Episodes of dominantly southerly swell usually lasted for a period of two to four days. This results in a strongly bimodal distribution of dominant wave direction. Owing to refraction the distribution of wave directions should be narrower at the nearshore gauge, though we were not able to obtain directional data with just one gauge.

4.4. Comparison of Wave Variables

[22] As measured by both the deep water buoy and nearshore wave gauge, southerly swells were typically longer period (10–14 s) than northerly swells (8–11 s) (Figure 4). Comparison of deep and shallow water records revealed a marked decrease in wave height during the transformation from a deep water wave to a shallow water wave. As energy density, E, is proportional to water density, ρ, gravity, g, and the square of wave height, H,

$$E = \frac{1}{8}\rho g H^2, \tag{1}$$

it decreased even more significantly during shoaling. The decrease was greatest for swells that come from azimuths less than 200° and greater than 260°, as these swells refract significantly prior to arriving at the Santa Cruz coast. We compute the fraction of deep water wave height that is maintained (Figure 4b). *Nelson and Leslighter* [1985] refer to this fraction as the energy transmission coefficient (K_t). If the effects of shoaling and refraction were minimal, the nearshore wave gauge would record the same wave height as the deep water buoy, and K_t would be 1.0. Periods of southwesterly (200°–260°) swell correspond to periods of highest preserved fractions of deep water wave height. More than 50% of the deep water wave height is preserved during southwesterly swell-dominated episodes (azimuths between

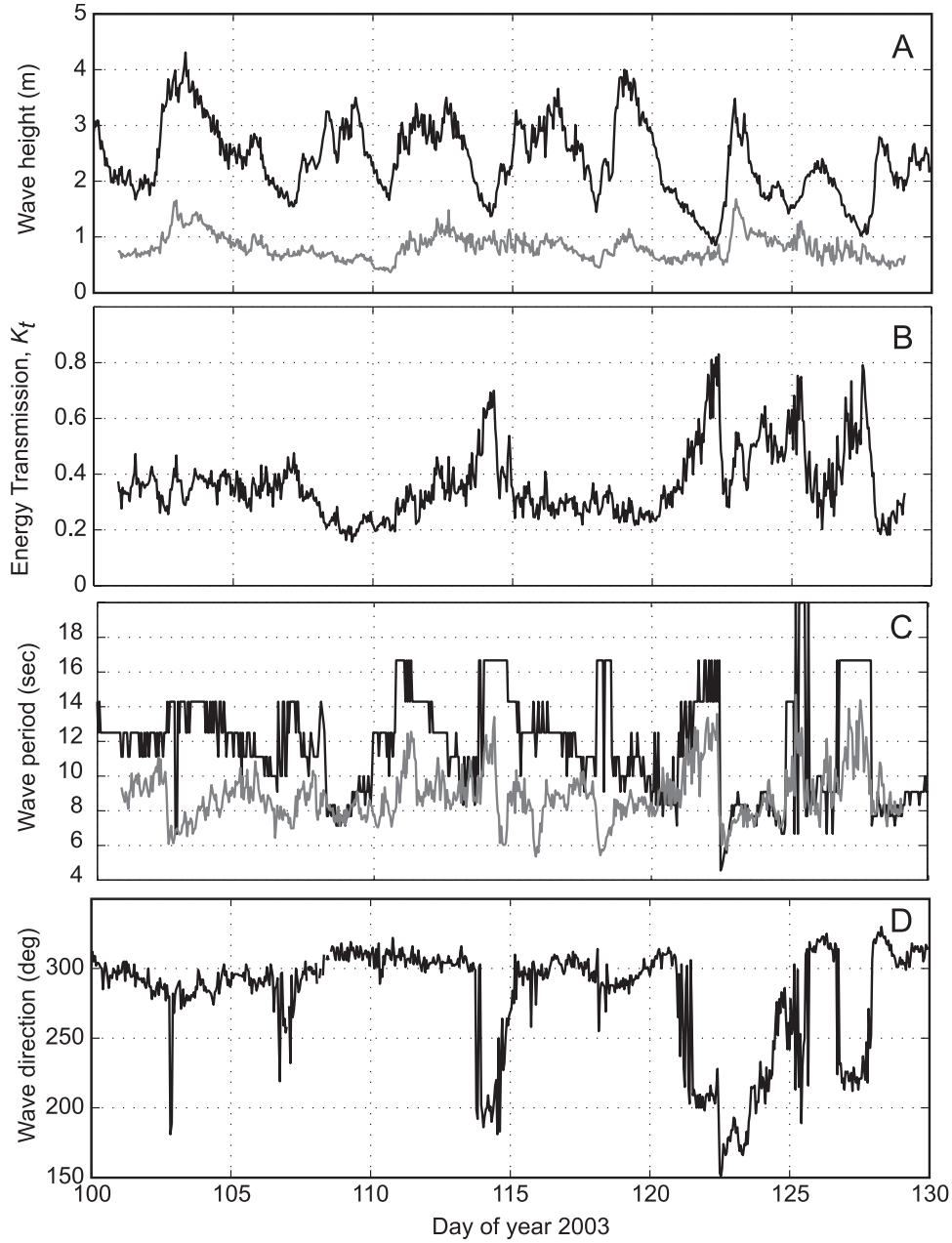

Figure 4. (a) Thirty day time series record of deep water (black line) and nearshore (shaded line) hourly significant wave height. (b) Corresponding record of energy transmission coefficient (K_t), representing the fraction of deep water wave height remaining in the nearshore environment (computed as H_n/H_d every hour). (c) Corresponding record of deep water (black line) and nearshore (shaded line) wave period. (d) Corresponding record of deep water wave direction.

200° and 260°). In addition, as wave period is positively correlated with the energy transmission coefficient, either the southwesterly swells are of longer period or longer period waves preserve energy more efficiently during transformation to a shallow water wave.

4.5. Microseismic Ground Velocity and Displacement

[23] The microseismic data are in the form of ground motion velocities sampled at 50 Hz. Sampling at this frequency for three directions of ground motion yields 540,000 data points per seismic instrument per hour. We devised the following strategy to analyze efficiently such a large data set and compare it with data from the nearshore wave gauge. First, each hour's worth of three-component velocity data is plotted and examined for quality to remove the confounding ground motions associated with earthquakes, joggers, and other anomalous disturbances. The data are high-pass filtered, with a cutoff frequency of 0.033 Hz (30 s) to ensure that we are not analyzing signals that have a longer period than the roll-off frequency of the seismometer, dictated by the instrument's frequency response curve.

[24] We show a representative series of contemporaneous velocity records of microseismic response to variations in

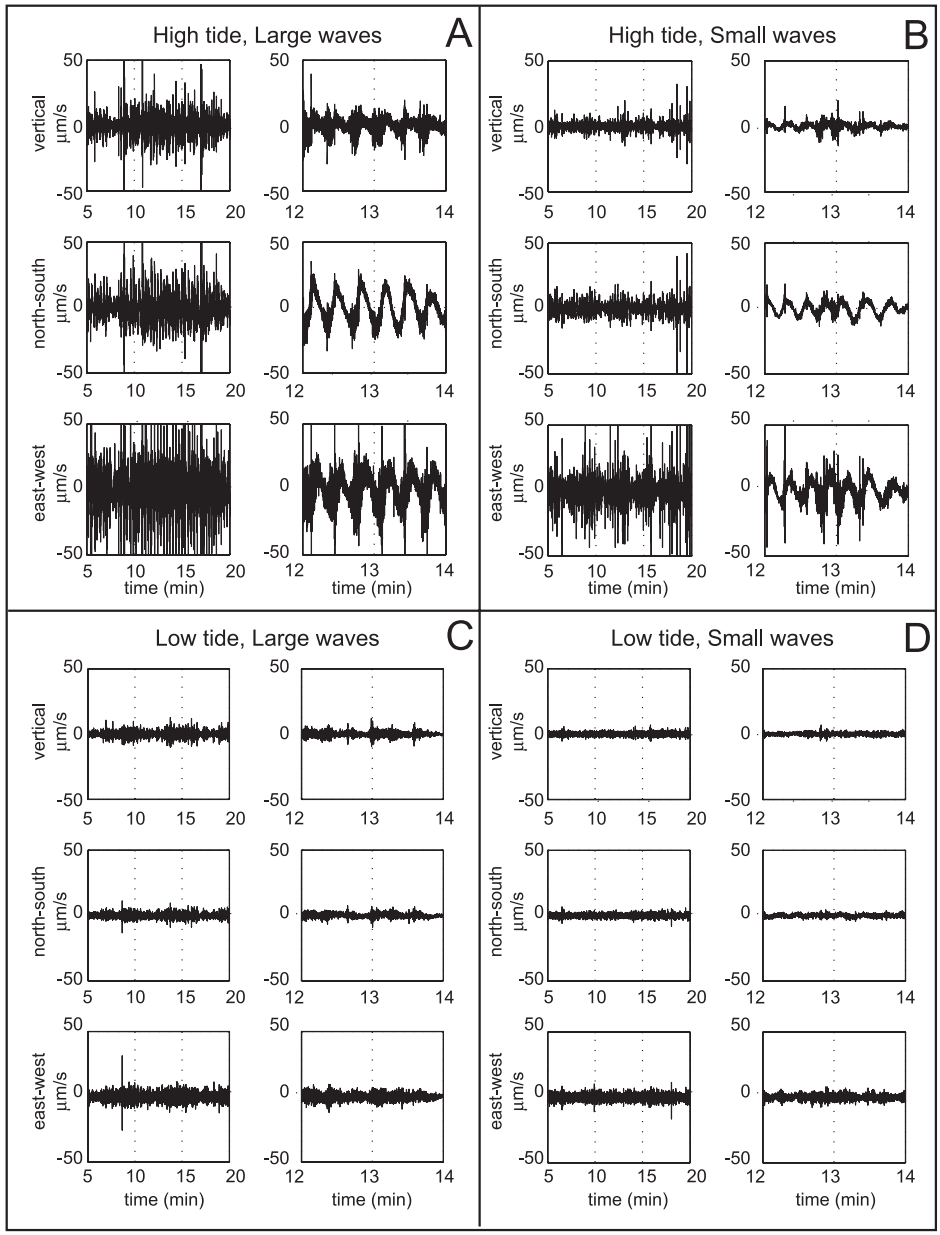

Figure 5. Samples of 15 and 2 min windows of three directions of ground motion velocity data from shoreward sensor. (a) High tide, large waves. (b) High tide, small waves. (c) Low tide, large waves. (d) Low tide, small waves. Note strong 10–20 s periodicity and high-frequency crashers riding along on the long-period sway.

tide and nearshore significant wave height for the seaward seismic station (SS-01) in Figure 5. The greatest variation in microseismic velocity occurred during periods of high tide and large wave heights for east-west ground motion at the shoreward sensor (SS-01). Predictably, the least variation in velocity occurred during low tides with small wave heights for all three directions of ground motion at the inland sensor (SS-02). During high tides, a 15–20 s periodicity is clearly visible in the velocity data from the seaward sensor (Figure 5), and is less prominent, although still present in the record from the inland sensor.

[25] We integrated the high-pass filtered velocity data to obtain displacements shown in Figure 6. Displacements are greatest for horizontal components of ground motion (north-south and east-west) at high tide during large wave heights, approaching amplitudes of 50 μm for the shoreward sensor. Greatest vertical displacements (during high tides and large wave events) for the shoreward sensor are 10 μm. Ground displacement is greatest during periods of high tide, chiefly during large swells, yet still significant during a period of more moderate swell height at the seaward sensor. The 15–20 s periodicity noticed in the velocity data is much cleaner and hence more clearly visible in the displacement data, at both the shoreward and inland sensors.

[26] We plot the particle motion observed by the shoreward and inland sensors during a single 15 min interval in Figure 7. The sea cliff sways simultaneously downward and toward the incoming wave field, mapping out a particle

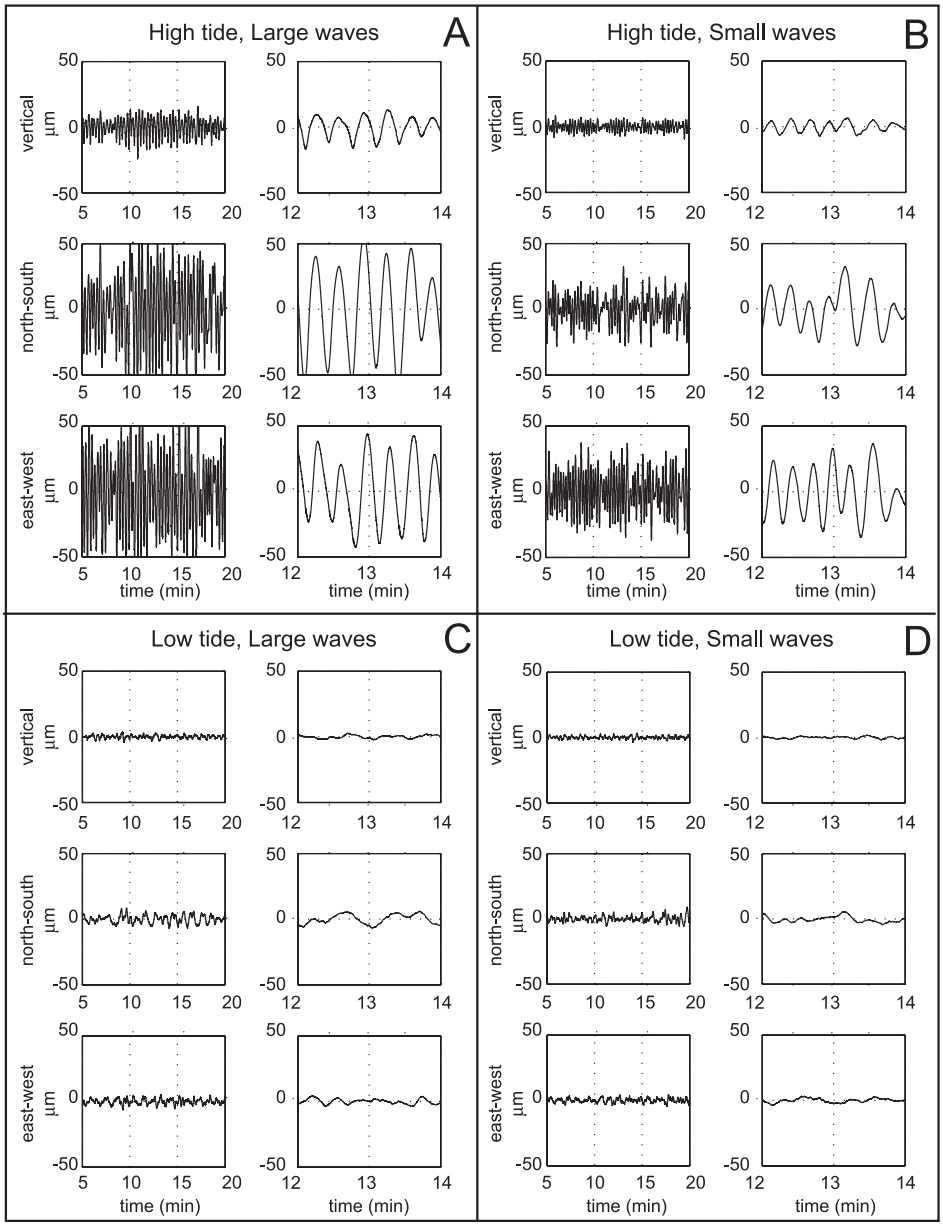

Figure 6. Samples of 15 and 2 min windows of three directions of ground motion displacement data from shoreward sensor at sea cliff edge. (a) High tide, large waves. (b) High tide, small waves. (c) Low tide, large waves. (d) Low tide, small waves. Displacements shown are computed by simply integrating the velocity data shown in Figure 5.

motion ellipsoid whose long axis is oriented roughly parallel with the nearshore wave direction. Although the particle motion pattern of the inland sensor is consistent with that of the shoreward sensor, the length of the maximum principal axis of the particle motion ellipsoid for the inland sensor is approximately 1/3 the length of the corresponding axis for the seaward sensor.

5. Discussion

[27] Given the simultaneous time series of microseismicity, deep water and nearshore wave conditions and tidal height, several obvious questions arise, and can be addressed: How do data from the wave gauge relate temporally to microseismic data of sea cliff shaking? What correlations exist between microseismic motions measured simultaneously by any two simultaneously recording sensors? What are the effects of a spatial gradient in microseismic sea cliff motion on long-term retreat rate?

5.1. Spectral Analysis

[28] To address the question of the relationship between the waves and the shaking, we have spectrally analyzed the time series from each source and compared them in the frequency domain. In Figure 8 we compare the power spectra of the nearshore wave gauge, and of the shoreward sea cliff shaking data for the four intervals whose

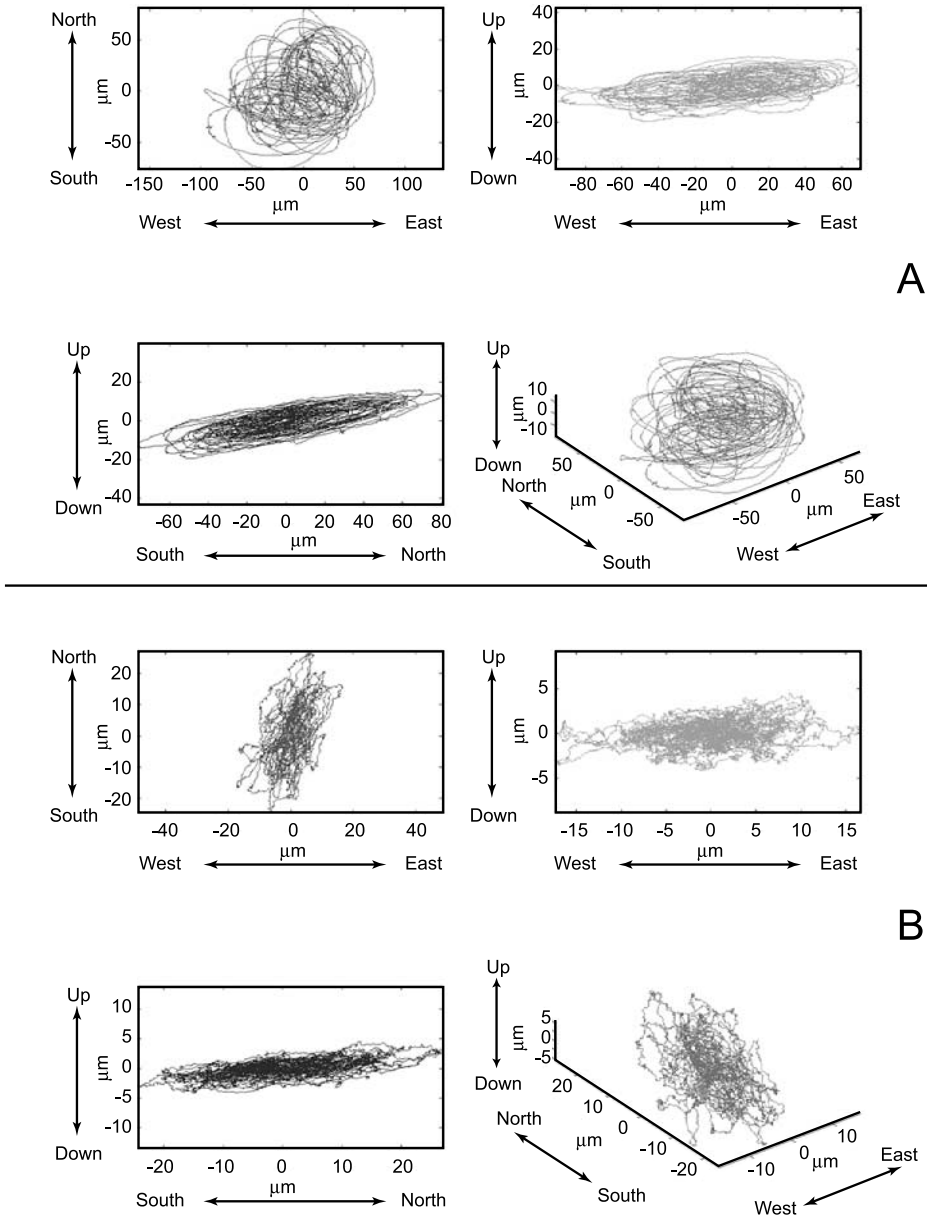

Figure 7. Simultaneous particle motion plots for (a) shoreward and (b) inland seismic sensors during a period of high tide and large waves, corresponding to velocity and displacement data of shoreward and inland seismic sensors. Note the dominance of horizontal motion (both east-west and north-south) as compared to vertical motion.

velocity and displacement data are shown in Figures 5 and 6, respectively. The top panel of each group on Figure 8 shows the power spectrum of the incoming wave field as measured by the nearshore wave gauge, while the lower three panels of each group show the spectra of the displacements in three directions of shaking recorded by the shoreward sensor. Remarkable agreement exists between the spectra during periods of high tide, irrespective of wave height (Figures 8a and 8b). The dominant periods of the incident wave field, as measured by the nearshore wave gauge, are spectrally indistinguishable from the dominant periods of sea cliff motion as measured by the seismometers. In contrast, during periods of low tide (Figure 8c and 8d), spectra are lower by one to two orders of magnitude and there is little correspondence between the wave gauge and the shaking spectra. However, Figures 8c and 8d show a significant amount of spectral power within the infragravity band (>20 s). Infragravity energy arises from the presence of edge waves, a common phenomenon in dissipative coastal environments and has been shown to dominate the periodicity of beach swash excursion studies [*Holman*, 1981; *Guza and Thornton*, 1982; *Holman and Sallenger*, 1985]. The spectral analyses suggest that microseismic sea cliff swaying, apparent on Figures 5a and 5b is strongly correlated with tidal height. Sea cliff swaying is most significant (10–100 μm), when the tidal level is above mean sea level, conditions that permit the incident

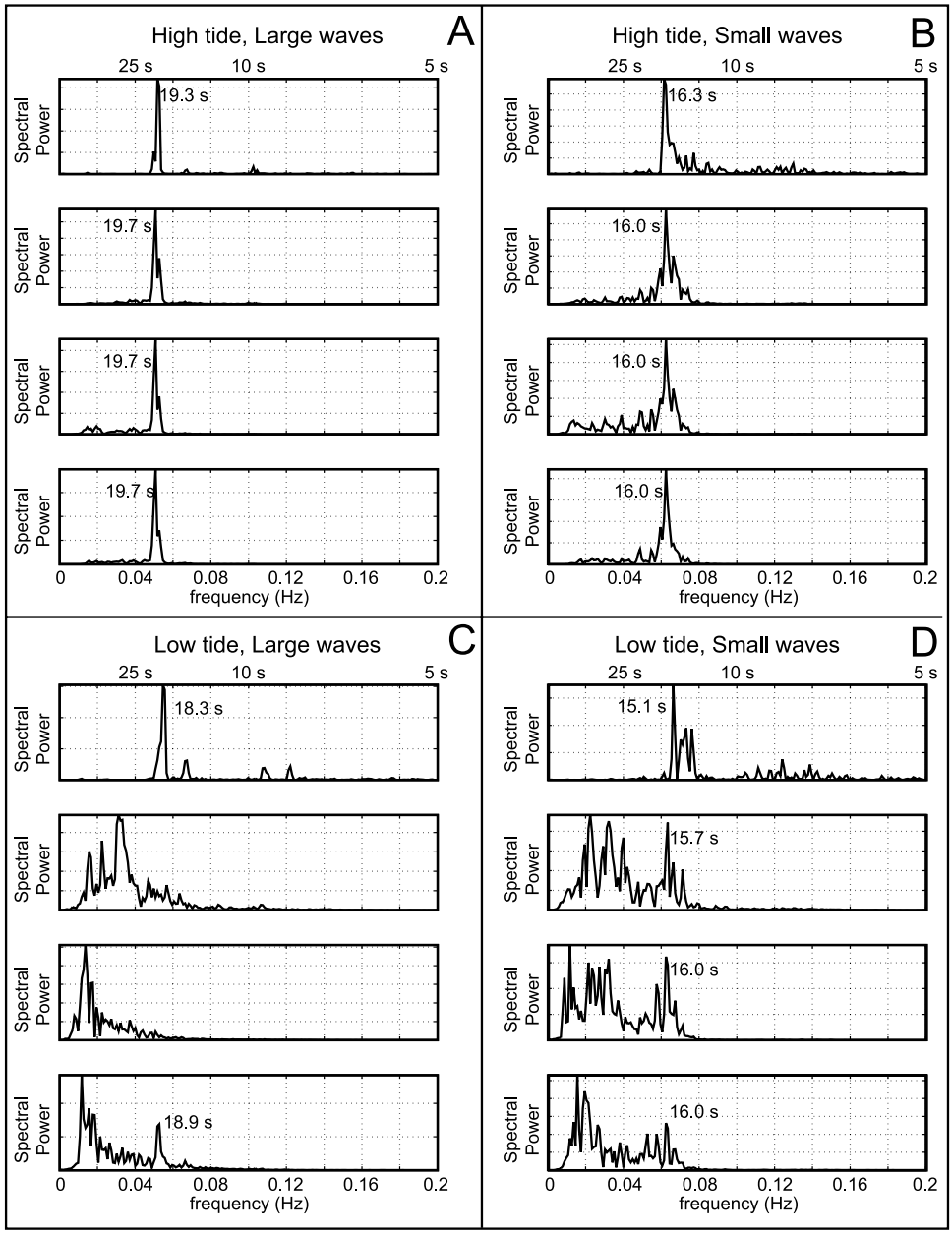

Figure 8. Spectral analyses of nearshore wave gauge water level data and microseismic displacement data from shoreward seismic station (SS-01) for the same time intervals shown in Figures 5 and 6. The top panel of each four-panel group is a spectral analysis of wave gauge data. The second, third, and fourth panels of each group are spectral analyses of vertical, north-south, and east-west microseismic displacements, respectively. (a) High tide, large waves. (b) High tide, small waves. (c) Low tide, large waves. (d) Low tide, small waves.

wave field to approach the base of the cliff, however, infragravity-driven motion occurs, to a lesser extent, at low tide.

[29] To explore this tide-related swaying more completely, we calculate spectrograms (time series plots of the power spectra) for the nearshore wave gauge data and the microseismic velocities as measured by the shoreward seismic station (Figure 9). Two distinct wave events from different source storms, emerge in the wave gauge spectrogram (Figure 9a) and appear to overlap for approximately one and a half days (day 124.5 to the beginning of day 126). Each of these wave events illustrates well the principle of wave propagation and energy conservation; long-period energy travels rapidly across the ocean and dissipates slowly, arriving at the distant shore prior to the shorter-period energy from the source region of storm generation. Using the second of these two distinct wave events as an example, we see that the first group of wave energy reaching the Santa Cruz wave gauge on day 124 is dominated by long-period waves (~20 s). The domi-

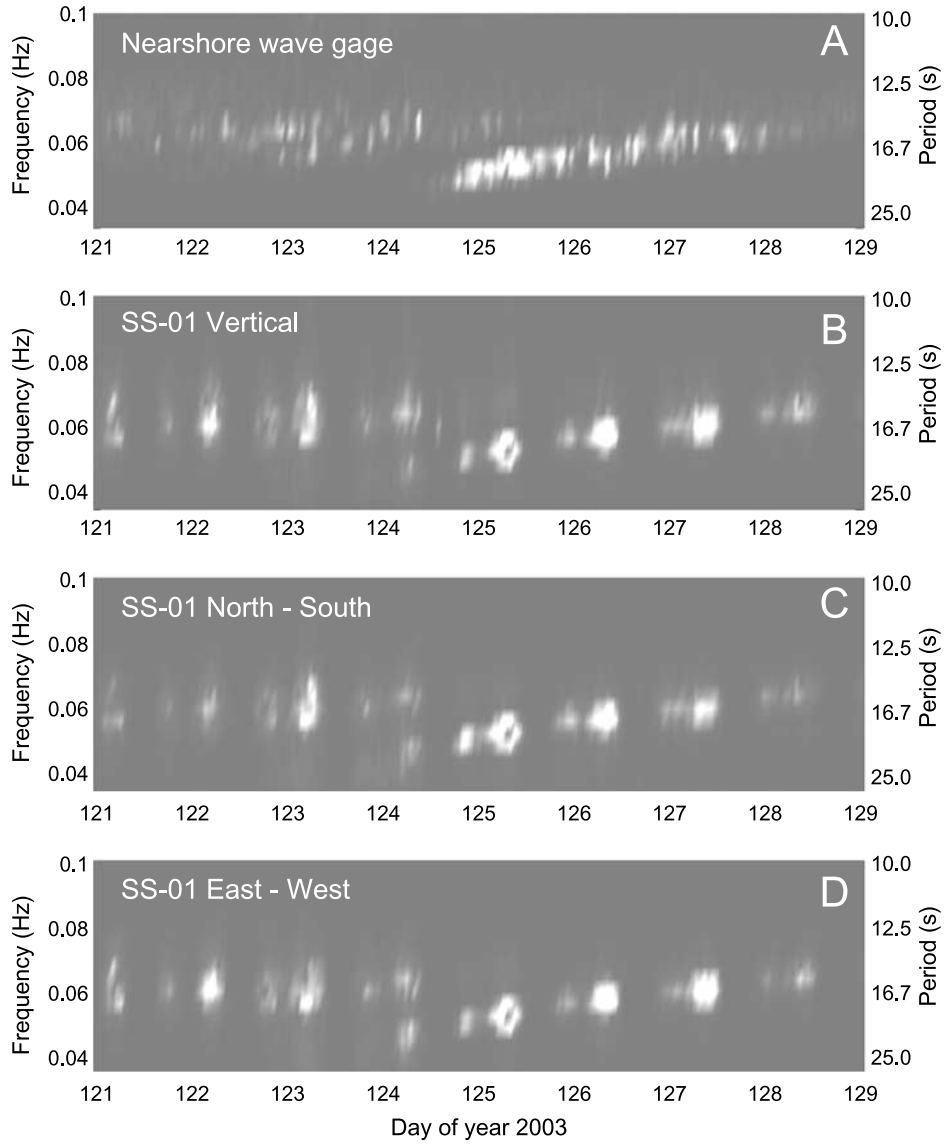

Figure 9. Spectrograms of (a) nearshore wave heights, (b) vertical microseismic velocities, (c) north-south microseismic velocities, and (d) east-west microseismic velocities. Note the spectrally powerful long-period signal of day 125 in each record and the semidiurnal beat of spectral power in the microseismic velocity spectrograms.

nant period of this wave event declines through the end of day 128, when most energy is in the 14–16 s band (0.06–0.07 Hz). The spectrograms of the microseismic data (Figures 9b–9d) also illustrate this shift from long-period shaking to shorter-period shaking as the wave event runs its course. The strongest peak in nearshore wave gauge spectral energy, on day 125, coincides with the strongest peak in microseismic velocity spectral energy for each of the three directions of ground motion. The semidiurnal modulation of spectral peaks in the microseismic velocity power spectra corresponds to periods of high tide, and more precisely to periods when the tidal level is above mean sea level. It is during these times that waves can transmit the most energy to the sea cliff. At these tidal levels the water is deeper, reducing wave energy dissipation through wave breaking processes supporting the conclusions of *Adams et al.* [2002].

5.2. Video Documentation

[30] While simultaneously collecting data from the shoreward seismic station (SS-01), we filmed a 1 hour interval of waves during which the tidal height was approximately mean sea level and the swell was small to moderate (~1.2 m in deep water). The video footage shows waves breaking 20–50 m from the base of the sea cliff. The broken wave bores then run up onto the wave cut platform directly in front of SS-01. Upon synchronizing the video clock with the seismic clock, it is evident that the onrush of the broken wave bore consistently matches the downward (2–15 μm (vertical)) and seaward (5–120 μm (north-south)) motion of

the sea cliff at the shoreward sensor (SS-01). This suggests a linked response of the shoreward portion of the marine terrace to the incoming wave field. In particular, it suggests that the cliff sways downward and outward as the wave breaks and rushes toward it. Having established that the displacement loop performed by the cliff top corresponds to the wave onrush, we now explore how this displacement changes with distance form the cliff edge.

5.3. Sea Cliff Strain

[31] Observations of the displacement data from the three seismic stations reveal a decrease in amplitude of sea cliff displacement with distance inland from the sea cliff edge. The sea cliff experiences both longitudinal (linear) strain, defined as the change in displacement over the original distance between two points,

$$\varepsilon_{xx} = \frac{\partial D_x}{\partial x}, \tag{2}$$

and shear strain, defined as the change in displacement in a direction normal to the line connecting two points, over that distance,

$$\varepsilon_{xy} = \frac{\partial D_y}{\partial x} \text{ or } \varepsilon_{xz} = \frac{\partial D_z}{\partial x}, \tag{3}$$

where D_x, D_y and D_z are the displacements in shore-normal (N-S), shore-parallel (E-W) and vertical, respectively. We must therefore assess the spatial gradients in measured displacements to obtain the pattern of strain.

[32] We plot a brief ($\sim$10 min) record of microseismic displacement in which we compare motion of the shoreward and midway sensors (Figure 10), and of the shoreward and inland sensors (Figure 11). When the seaward portion of the cliff moves a particular direction, that motion is mimicked in phase by the midway and inland portions, but with reduced amplitude. The consistent patterns of strong gradients in the displacements suggest that the first few tens of meters of the rock mass experience a measurable, periodic strain induced by the waves.

[33] We distill each hour of microseismic displacement data into a characteristic displacement value (CDV) that we define to be the width of the envelope that captures ±2 standard deviations (95%) of the displacement data for that hour. The difference between shoreward and inland CDVs divided by the distance between sensors SS-01 and SS-02 represents longitudinal and shear strains, as defined above (equations (2) and (3)). The time series of shoreward CDVs, inland CDVs, and the strain generated by their differences, are plotted along with the tide and nearshore wave heights for days 120 through 147 (30 April–27 May 2003) in Figure 12. Both the shoreward and inland CDVs vary considerably, but are obviously in phase with tidal fluctuations, and less obviously in phase with periods of large wave height. As the seismic sensors are oriented along a north-south line, any strain in the north-south direction is treated as a longitudinal strain (taken to be positive if elongation). Strains calculated in the east-west and vertical directions are perpendicular to the line connecting the seismic sensors, and are therefore shear strains. Greatest strains, like the displacements, are recorded for horizontal motion, as opposed to the vertical motion.

[34] The CDV pattern and its derivative, the strain, may be used to constrain a continuous pattern of strain within the bedrock of the sea cliff. We define the displacement amplitude ratio

$$AR = \frac{D_i}{D_o} \tag{4}$$

for an hour of observation as the quotient of the displacement at an interior location, D_i, divided by the displacement at the sea cliff edge, D_o. For the interior location displacements, D_i, we use the CDVs from either the inland or the midway seismic station (SS-02 or SS-03), depending upon which is operational at the time. For the sea cliff edge displacements, D_o, we use the CDVs from the shoreward seismic station (SS-01). By definition, AR at the shoreward station, for any direction of ground motion, must be 1.0. The AR values are plotted in Figure 13, and map out the strain profiles within the bedrock of the marine terrace. We show for comparison exponential relationships of the form

$$\mathrm{AR} = \frac{D}{D_o} = e^{-x/x^*}, \tag{5}$$

where x is the distance inland from the seaward sensor (SS-01), and x^* is a characteristic distance over which the amplitude decays. Exponentials are fit to midtide AR values for each of the three directions of ground motion. We distribute the hourly AR values for each seismic station and each direction of ground motion into 3 equally spaced tidal bin categories (high tide = +1.08 m to +0.24 m, midtide = +0.24 m to −0.60 m, and low tide = −0.60 m to −1.44 m). The midtide values for x^* ($x^*_{ud,mt}$ = 30.2 m, $x^*_{ns,mt}$ = 28.5 m, $x^*_{ew,mt}$ = 30.2 m) represent the distance inland from the sea cliff edge where the amplitude has diminished to $1/e$ of its value at the seaward sensor, averaged over the tidal range. We obtain similar values for x^* for AR values put into low-tide and high-tide bins ($x^*_{ud,lt}$ = 41.7 m, $x^*_{ns,lt}$ = 42.7 m, $x^*_{ew,lt}$ = 39.2 m, $x^*_{ud,ht}$ = 24.2 m, $x^*_{ns,ht}$ = 26.2 m, $x^*_{ew,ht}$ = 17.3 m). As the cliff height is roughly 10 m, these length scales are on the order of two to three cliff heights. By many ($\sim$10) cliff heights from the coast, here roughly 100 m, the rock mass does not experience significant strain associated with the wave loading cycle. The consistency of the characteristic length scale, x^*, for all types of displacement at each of two tidal conditions suggests that we may now cast the pattern of longitudinal strain as

$$\varepsilon_{xx} = \frac{dD_x}{dx} = \frac{d}{dx}\left(D_{xo}e^{-x/x^*}\right) = -\frac{D_{xo}}{x^*}e^{-x/x^*} \tag{6}$$

and that for shear strains as

$$\varepsilon_{xy} = \frac{dD_y}{dx} = \frac{d}{dx}\left(D_{yo}e^{-x/x^*}\right) = -\frac{D_{yo}}{x^*}e^{-x/x^*}$$

or

$$\varepsilon_{xz} = \frac{dD_z}{dx} = \frac{d}{dx}\left(D_{zo}e^{-x/x^*}\right) = -\frac{D_{zo}}{x^*}e^{-x/x^*}. \tag{7}$$

[35] The magnitude of the strains is therefore set by the magnitude of the displacements at the sea cliff, and the

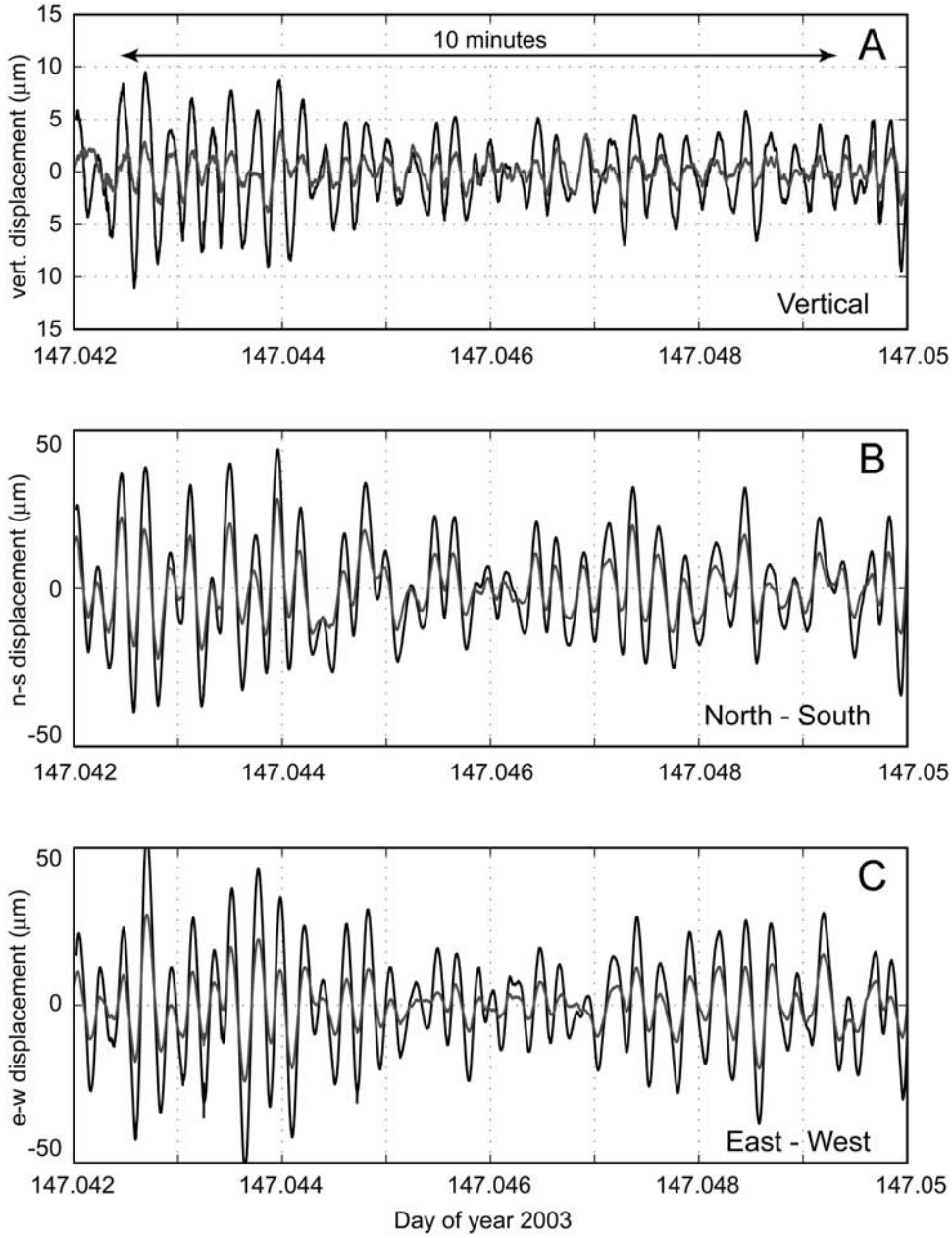

Figure 10. Ten min time series comparison of displacement data from shoreward seismic station (SS-01, shown in gray) and midway seismic station (SS-03, shown in black) for (a) vertical, (b) north-south, and (c) east-west directions of ground motion.

length scale we have just constrained. As the amplitude of the characteristic displacements at SS-01 are 27, 122, and 137 μm, and at SS-02 are 13, 39, and 30 μm (Figure 12), and the length scale for the decay of displacement with distance from the cliff edge is ~ 30 m, the maximum strains to which a rock mass is subjected during a flexing cycle are ~0.5, 2.8, and 3.6 μstrain for vertical, north-south, and east-west motion, respectively.

[36] The rapid decay of displacement amplitude with distance from the sea cliff reinforces our argument that the waves induce the motion by periodic loading of the nearshore with each wave. Assuming an average wave period of ~10 s, this amounts to over three million cycles of sea cliff flexing per year, each of which induces a few μstrain.

5.4. Process Implications

[37] What role does this periodic straining of the rock mass play in the long-term rate of sea cliff retreat in rocky coastal environments? We propose that this repeated strain weakens rock by facilitating crack initiation and propagation, which in turn prepares the rock for quarrying of blocks when the rock is finally exposed at the sea cliff face.

[38] Cyclic loading by waves induces the ground motions shown in Figure 7. The three-dimensional ground motion pattern for any one wave-loading cycle is approximately a

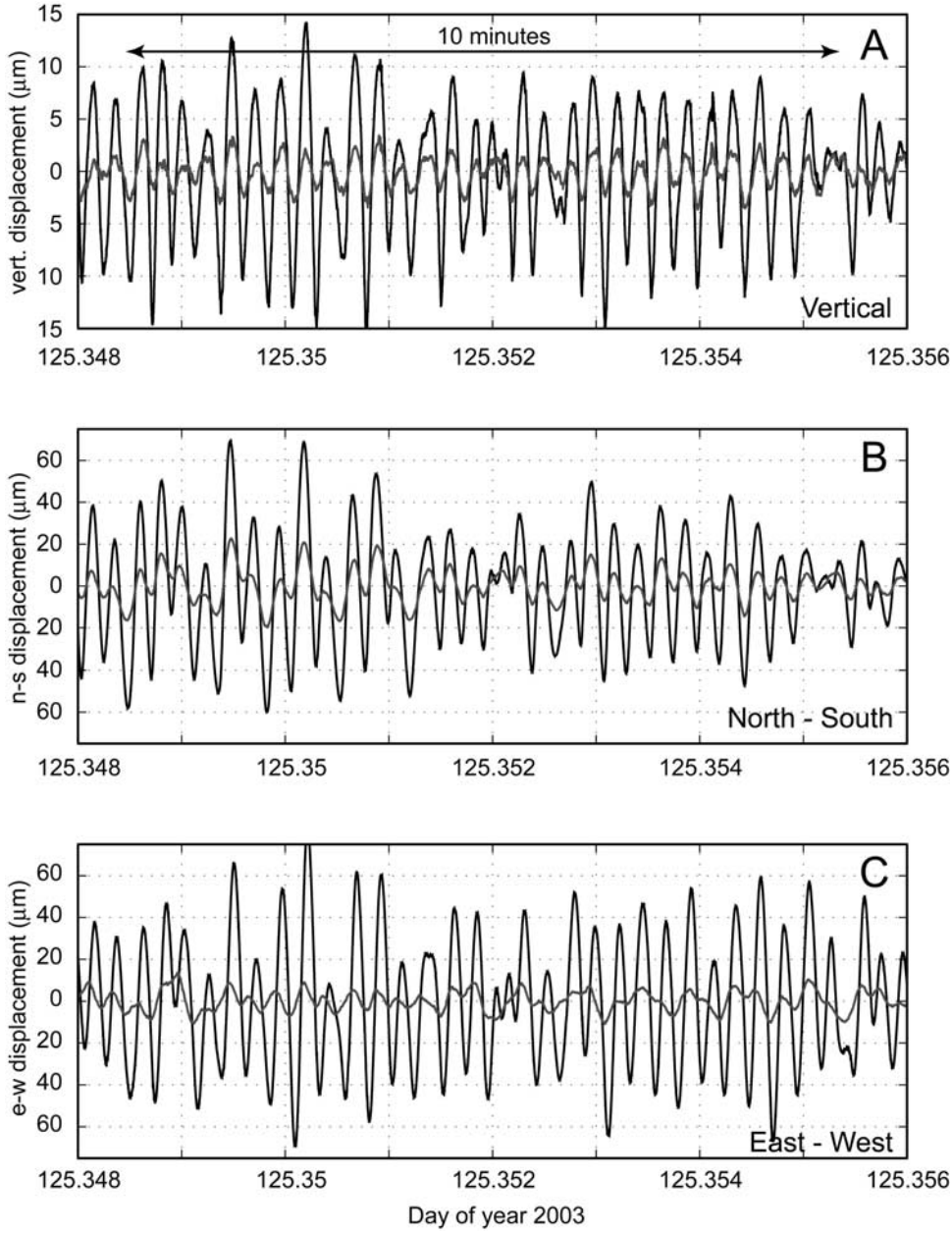

Figure 11. Ten min time series comparison of displacement data from shoreward seismic station (SS-01, shown in gray) and inland seismic station (SS-02, shown in black) for (a) vertical, (b) north-south, and (c) east-west directions of ground motion.

closed circle, as the seismic sensor returns to its original position. However, cyclic loading is known to reduce the effective strength of a material and to advance the time of failure. Research in experimental rock mechanics and material strength utilizes a failure strength-loading cycles curve (typically referred to as an "*S*-*N* curve") which documents the exponential decay in the failure limit of a material (*S*) with increasing number of loading cycles (*N*) [*Horibe et al.*, 1970; *Brighenti*, 1979]. The high-stress portion of a loading cycle promotes tensile failure and opening of microfissures owing to the high-stress intensity at crack tips [*Goodman*, 1989]. As the rock does not heal in the low-strain portion of the loading cycle, damage accumulates even in the face of perfectly symmetrical loading, and the yield strength of the rock declines: it can fail at some fraction of its prestressed strength. Water saturation enhances the effect of cyclic loading, as compressed water within the confined pore spaces exerts higher outward pressures during loading than does trapped air [*Goodman*, 1989]. The sea cliff face is often wet, either due to wave splash or the seepage of ground water, suggesting that the saturation enhancement of loading-induced fatigue may be of significant importance. This has also been suggested to play a role in vertical bedrock erosion under oscillatory waves [*Davidson-Arnott*, 1986].

[39] We may calculate the effect of wave-induced cyclic loading by knowing the maximum strain per cycle and estimating the unconfined strength and elastic modulus of

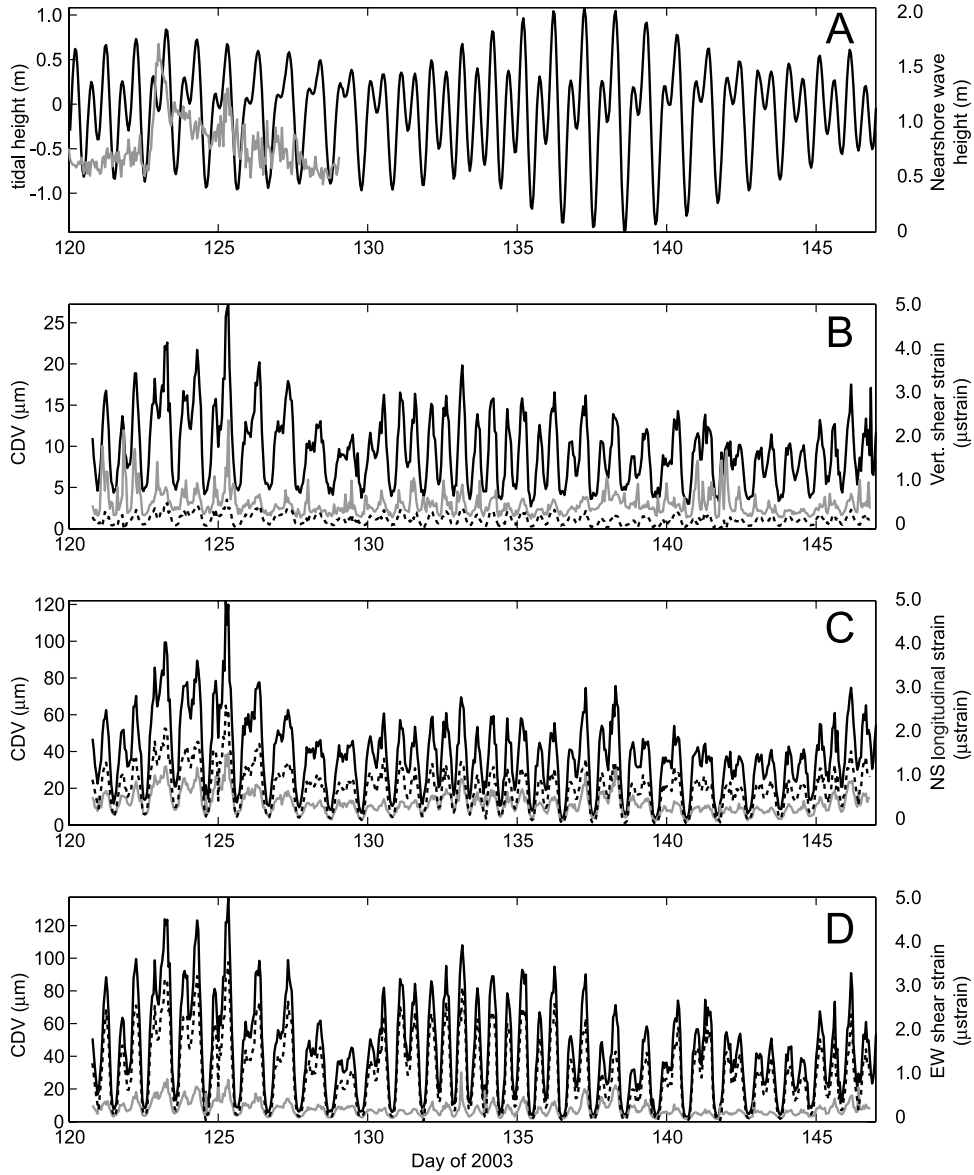

Figure 12. Time series of tide, nearshore wave heights, characteristic displacement values for shoreward and inland sensors, and strain calculations derived from displacement differences between stations SS-01 and SS-02. (a) Tidal height (black line) and nearshore wave heights (shaded line). (b) Vertical shoreward and inland characteristic displacement values (CDVs) (black and shaded lines, respectively) and vertical shear strain (dashed line). (c) North-south shoreward and inland CDVs (black and shaded lines, respectively) and north-south longitudinal strain (dashed line). (d) East-west shoreward and inland CDVs (black and shaded lines, respectively) and east-west shear strain (dashed line).

the sea cliff rock. Using a simplified form of an equation provided by *Jafari et al.* [2003], the reduced (fatigued) failure strength of the rock mass, τ_f, may be estimated using

$$\tau_f = \tau_p e^{\frac{-N}{N_0}} e^{\frac{-\tau_c}{\tau_p}}, \tag{8}$$

where τ_p is the pristine rock failure strength, N is the number of loading cycles experienced by the sea cliff, N_0 is a characteristic number of loading cycles (a property describing rock fatiguing behavior), and τ_c is the maximum stress experienced during a loading cycle. This maximum stress is estimated from

$$\tau_c = E\varepsilon_c, \tag{9}$$

where E is Young's modulus of the rock mass (herein set to 20 GPa, a typical value for mudstone), and ε_c is the maximum strain experienced in a loading cycle (0.5, 2.8, and 3.6 μstrains, for vertical, north-south, and east-west ground motions, respectively). We assume the pristine rock failure strength to be the unstressed uniaxial tensile failure strength for mudstone, typically 10 MPa (10^4 kPa). Given the small strains we have documented, and hence the small

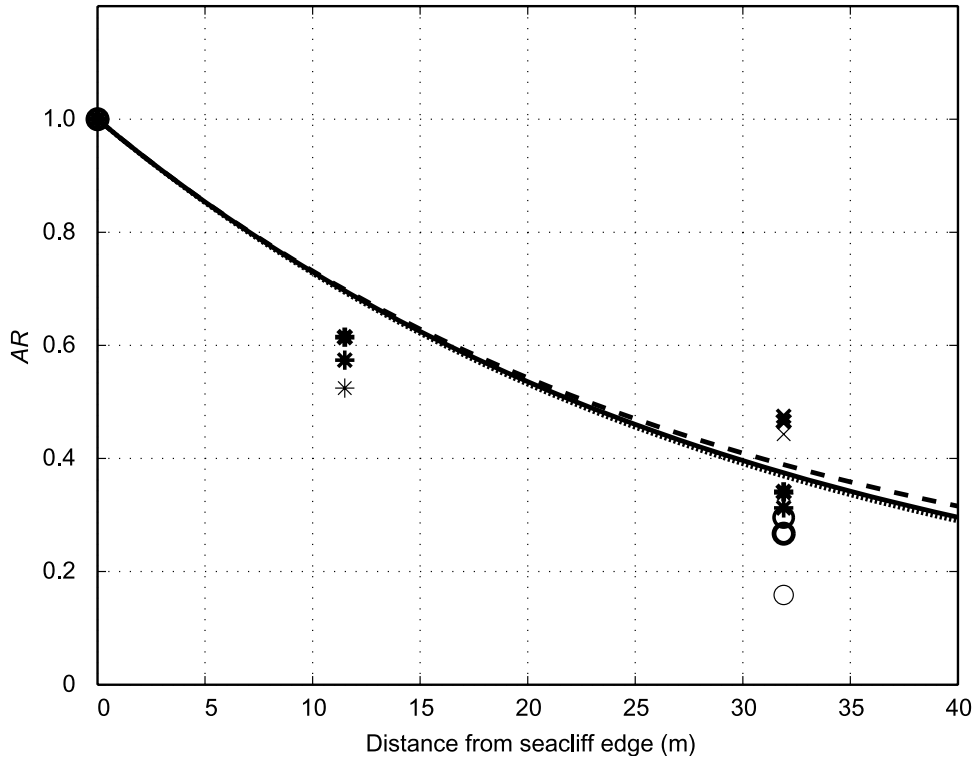

Figure 13. Spatial profile of displacement amplitude ratios (AR) derived from the midway (~11 m) and inland (~32 m) seismic stations. Bold, medium, and light markers correspond to vertical, north-south, and east-west directions of ground motion, respectively. Circles represent high-tide ARs, asterisks represent midtide ARs, and crosses represent low-tide ARs. Curves are exponential fits to midtide values (solid line, vertical; dashed line, north-south; dotted line, east-west).

stress per loading cycle, the contribution from the second exponential in equation (8) is negligible. The fatigue arises primarily from the number of cycles experienced by the sea cliff - the first exponential in equation (8). Figure 14 is a normalized *S-N* curve constructed to demonstrate the deterioration of failure strength for sea cliff bedrock assuming a consistent wave field, homogeneous lithology, and strain conditions similar to those experienced by the Santa Cruz sea cliffs. After N_0 loading cycles, the material strength has declined to $1/e$ of its original strength. While we do not know what this characteristic number of cycles is for Santa Cruz mudstone, given that it experiences on the order of a billion cycles of significant amplitude before it is exposed at the sea cliff, if N_0 is on this order or smaller, the effect of cyclic loading will have served to reduce the material strength of the rock significantly. We propose that this process is the weakening mechanism. Failure, and hence cliff retreat, likely occurs through the strong shaking associated with direct wave impact, as documented in our earlier study of high-frequency shaking [*Adams et al.*, 2002]. Failure likely occurs earlier during an anomalous storm event that provides much larger incident waves that impact the sea cliff with high stresses.

5.5. Strain History

[40] In light of the potential of sea cliff bedrock fatigue highlighted by the preceding discussion, we now discuss the long-term effects of this process on the geomorphic evolution of a rocky coast. For the north shore of Monterey Bay, estimates of spatially and temporally averaged rate of sea cliff retreat during the current sea level high stand range from 7 to 15 cm/yr [*Moore and Griggs*, 2002], to approximately 30 cm/yr [*Griggs and Savoy*, 1985], for sea cliffs cut into Purisima Sandstone. Sea cliffs cut into the Santa Cruz Mudstone, such as those at the Long Marine Lab study site, are probably retreating more slowly [*Griggs and Johnson*, 1979; *Best and Griggs*, 1991]. Expanding our midtide AR flexure curve of Figure 13 to an actual characteristic displacement value (CDV) flexure curve, we obtain profiles of displacement and strain through which an inland rock parcel would migrate as the sea cliff face marches landward (Figure 15). We approximate the strain history of a rock parcel while within the "damage accumulation zone" (Figure 15) using (1) a reasonable sea cliff retreat rate of 10 cm/yr, (2) a mean wave period of 10 s, and (3) the CDV curves of Figure 15. The rock parcel would witness approximately 5.4 km of vertical, 23.6 km of north-south, and 23.6 km of east-west ground motion through the course of approximately 1 billion flexing cycles over ~300 years. While zero net motion is accomplished owing to the closed displacement paths, we argue that the rock is nonetheless damaged in the process. In Figure 16 we illustrate schematically how this sea cliff flexing mechanism might serve to accumulate strain, and hence damage, in the bedrock of the lowest emergent marine terrace. A rock parcel enters the sea cliff boundary zone of order 100 m width (many x^*, each being order two cliff heights), and begins to accumulate strain slowly. As the sea cliff retreats,

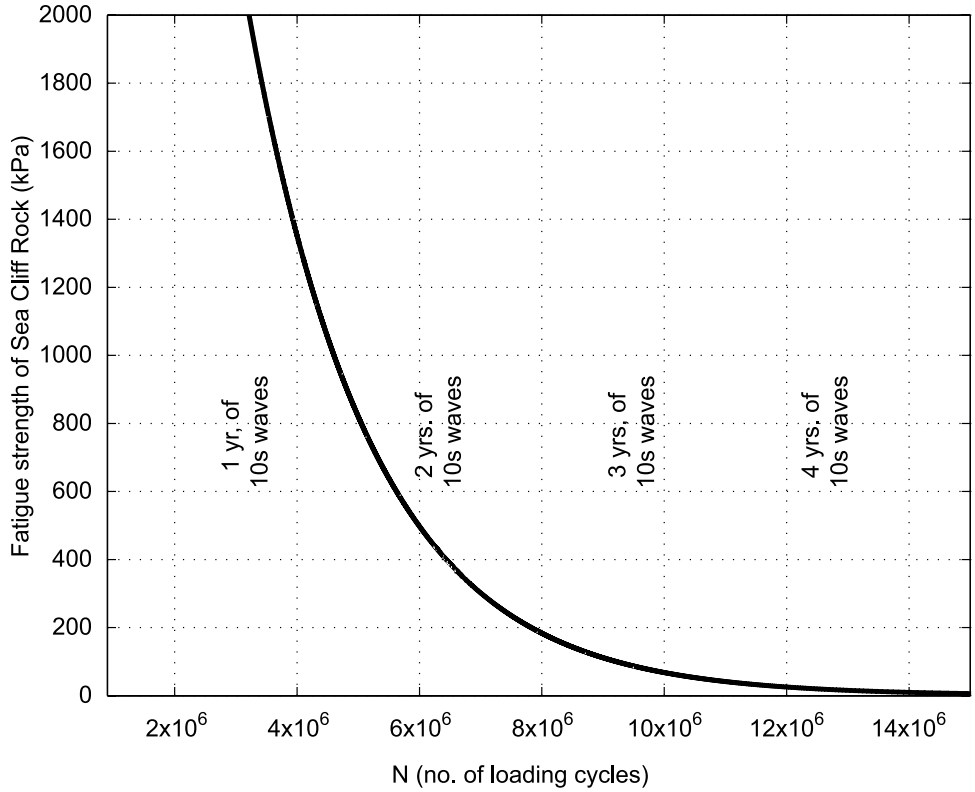

Figure 14. Hypothetical *S-N* curve for Mudstone of the Santa Cruz sea cliffs, estimated using equation (8), a steady uniform wave field, the local sea cliff retreat rate, maximum measured strains in this study, and typical values for unstressed tensile strength and Young's elastic modulus for mudstone.

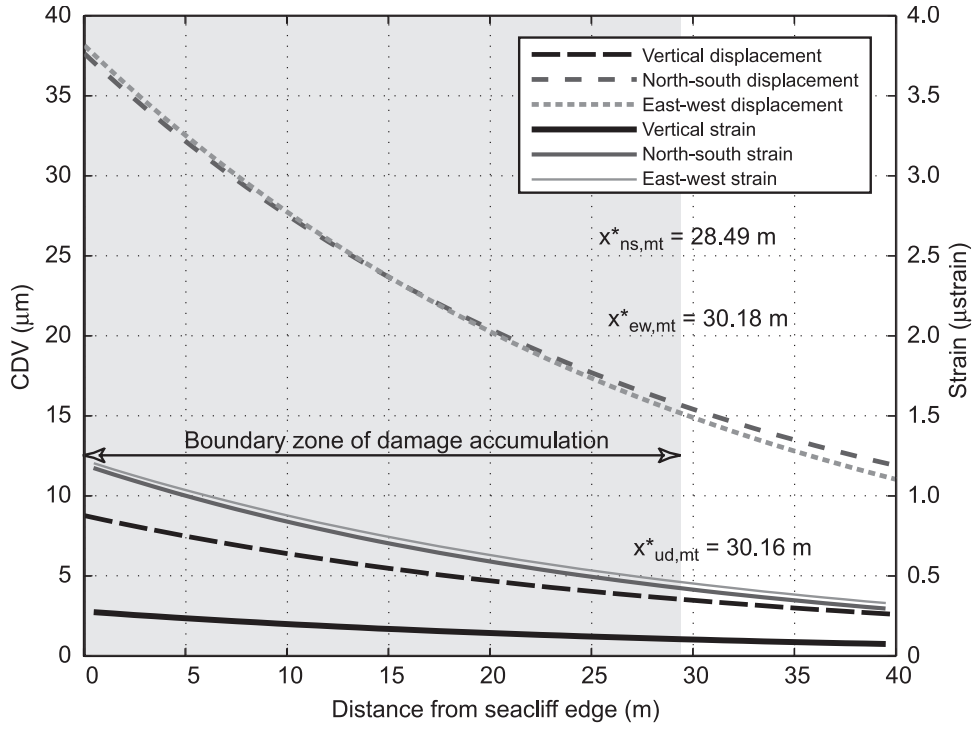

Figure 15. Exponential fits to the CDV profiles and accompanying strain profiles for each direction of ground motion. These curves represent the absolute displacements that the bedrock witnesses, with each wave-induced flexure of the sea cliff.

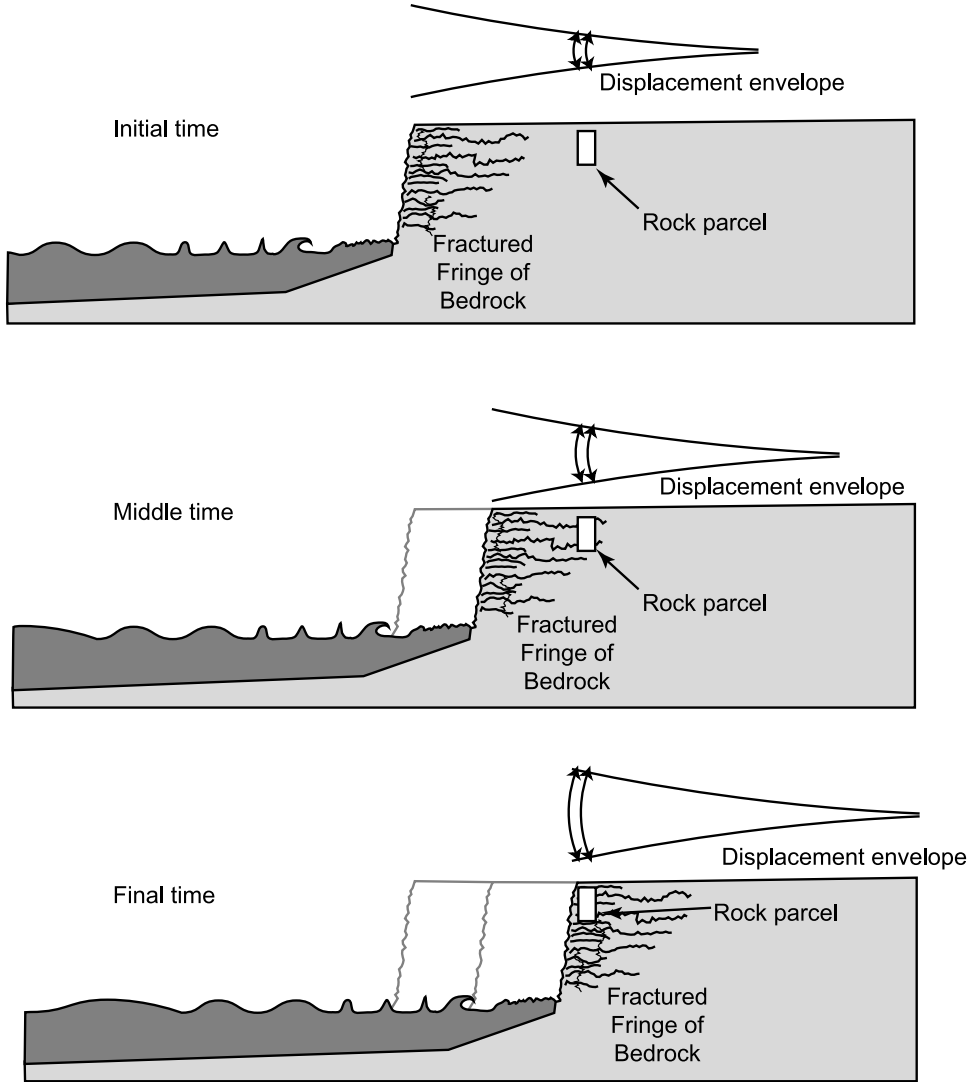

Figure 16. Schematic illustrating our conceptual model for the displacement and strain history witnessed by a parcel of bedrock within the marine terrace. As sea cliff retreat brings the cliff face progressively closer to the tracked rock parcel, the parcel experiences greater displacements and greater strain until finally becoming exposed to direct wave attack and block removal from the cliff face.

the strain envelope moves landward, causing the same parcel of rock to accumulate strain (or damage) at a greater rate, reducing its strength more rapidly. Finally, in the lower panel of Figure 16, the cliff face has reached our parcel of rock, which is now experiencing the greatest strain, and is therefore losing strength most rapidly. This cyclical accumulation of damage prepares the sea cliff for block failure-style erosion, a process tied to the high-frequency sea cliff shaking reported by *Adams et al.* [2002]. In essence, sea cliff retreat may result from a combination of a long-period swaying of the rock mass that loosens bedrock by initiation and propagation of cracks, and short-period shaking that promotes the removal of the resulting blocks from the cliff face.

6. Conclusions

[41] Simultaneous measurements of nearshore waves and microseismic ground motions of sea cliff bedrock have provided evidence that wave loading of the intertidal zone induces periodic motion in the onshore marine terrace bedrock. Spectral analyses of the seismic records, and video documentation of wave loading, confirm that the microseismic displacements are caused by the incident waves. Multiple seismic stations arrayed normal to the coastline reveal that the amplitude of the wave-induced displacements falls off exponentially with distance from the cliff, resulting in strain within the bedrock of the sea cliff of up to four microstrains per wave-loading cycle. We propose that this cyclical loading fatigues sea cliff bedrock by microcracking, lowering the bedrock failure strength, thereby making the cliff face more susceptible to several erosional processes upon exposure to direct wave attack, most of them associated with direct wave impact [e.g., *Adams et al.*, 2002].

[42] **Acknowledgments.** We are indebted to Gary Griggs (LML director), who first offered Long Marine Lab as a field site, and to Steve Davenport (LML manager), who offered on-site support and enthusiasm for

our project. Dan Sampson and Eli Morris provided much needed help with the seismometer setup and troubleshooting problems with the data collection. We thank the Southern California Earthquake Center and Aaron Martin, who generously loaned us the portable broadband seismometers and instructed P.N.A. in their use. Mike Field loaned wave gauges that provided most of the nearshore oceanographic data. Mike Loso shared his knowledge of GPS mapping to help create a high-resolution DEM of the field area. Josh Logan assisted with GIS work. We thank Patrick Barnard, Bruce Richmond, two anonymous reviewers, and the Editors for their comments on the manuscript. Financial support for this research came from a Friends of the Long Marine Lab grant to P.N.A. and from an NSF grant to R.S.A. (NSF-EAR-0003604).

References

Adams, P. N., R. S. Anderson, and J. Revenaugh (2002), Microseismic measurement of wave-energy delivery to a rocky coast, *Geology*, *30*, 895–898.

Bagnold, R. A. (1939), Interim report on wave pressure research, *J. Inst. Civ. Eng.*, *12*, 202–226.

Best, T. C., and G. B. Griggs (1991), A sediment budget for the Santa Cruz littoral cell, California, in *From Shoreline to Abyss*, spec. publ., pp. 35–50, Soc. for Sediment. Geol., Golden, Colo.

Birkemeier, W. A., C. F. Baron, M. W. Leffler, K. K. Hathaway, H. C. Miller, and J. B. Strider (1989), SUPERDUCK nearshore processes experiment data summary: CERC Field Research Facility, *Misc. Pap. CERC-89-16*, U.S. Army Corps of Eng., Washington, D. C.

Bormann, P., and E. Bergman (2002), *New Manual of Seismological Observatory Practice*, Global Seismological Services, Golden, Colo.

Bradley, W. C., and G. B. Griggs (1976), Form, genesis, and deformation of central California wave-cut platforms, *Geol. Soc. Am. Bull.*, *87*, 433–449.

Brighenti, G. (1979), Mechanical behavior of rocks under fatigue, paper presented at the 4th Congress, Int. Soc. Rock Mech., Montreaux, Switzerland.

Bromirski, P. D. (2001), Vibrations from the "Perfect Storm", *Geochem. Geophys. Geosyst.*, *2*, doi:10.1029/2000GC000119.

Bromirski, P. D., and F. K. Duennebier (2002), The near-coastal microseism spectrum: Spatial and temporal wave climate relationships, *J. Geophys. Res.*, *107*(B8), 2166, doi:10.1029/2001JB000265.

Bromirski, P. D., R. E. Flick, and N. Graham (1999), Ocean wave height determined from inland seismometer data: Implications for investigating wave climate changes in the NE Pacific, *J. Geophys. Res.*, *104*, 20,753–20,766.

Chin, J. L., J. R. Morrow, C. R. Ross, and H. E. Clifton (1993), Geologic maps of the upper Cenozoic deposits in central California, in *U.S. Geol. Surv. Misc. Invest. Ser. Map*, *I-1943*.

Davidson-Arnott, R. G. D. (1986), Rates of erosion of till in the nearshore zone, *Earth Surf. Processes Landforms*, *11*, 53–58.

Dupre, W. R. (1984), Reconstruction of paleo-wave conditions during the late Pleistocene from marine terrace deposits, Monterey Bay, California, *Mar. Geol.*, *60*, 435–454.

Goodman, R. E. (1989), *Introduction to Rock Mechanics*, 562 pp., John Wiley, Hoboken, N. J.

Greene, H. G. (1977), Geology of the Monterey Bay region, in *U.S. Geol. Surv. Open File Rep.*, *77-0718*, 343 pp.

Greene, H. G., and J. C. Clark (1979), Neogene paleogeography of the Monterey Bay area, CA, paper presented at the 3rd Pacific Coast Paleogeography Symposium, Soc. for Sediment. Geol., Los Angeles, Calif.

Grevemeyer, I., R. Herber, and H. H. Essen (2000), Microseismological evidence for a changing wave climate in the northeast Atlantic Ocean, *Nature*, *408*, 349–352.

Griggs, G. B., and R. E. Johnson (1979), Coastal erosion Santa Cruz County, *Calif. Geol.*, *32*, 67–76.

Griggs, G., and L. Savoy (1985), *Living With the California Coast*, 393 pp., Duke Univ. Press, Durham, N. C.

Guza, R. T., and E. B. Thornton (1982), Swash oscillations on a natural beach, *J. Geophys. Res.*, *87*, 483–491.

Hapke, C., and B. Richmond (2002), The impact of climatic and seismic events on the short-term evolution of seacliffs based on 3-D mapping: Northern Monterey Bay, California, *Mar. Geol.*, *187*, 259–278.

Haubrich, R. A., W. H. Munk, and F. E. Snodgrass (1963), Comparative spectra of microseisms and swell, *Bull. Seismol. Soc. Am.*, *53*, 27–37.

Holman, R. A. (1981), Infragravity energy in the surf zone, *J. Geophys. Res.*, *86*, 6442–6450.

Holman, R. A., and A. H. J. Sallenger (1985), Set-up and swash on a natural beach, *J. Geophys. Res.*, *90*, 945–953.

Horibe, T., R. Kobayashi, and Y. Ikemi (1970), Fatigue test of rocks, paper presented at the 3rd Japan Symposium on Rock Mechanics, Jpn. Comm. of Rock Mech., Tokyo.

Jafari, M. K., K. A. Hosseini, F. Pellet, M. Boulon, and O. Buzzi (2003), Evaluation of shear strength of rock joints subjected to cyclic loading, *Soil Dyn. Earthquake Eng.*, *23*, 619–630.

Komar, P. D. (1998), *Beach Processes and Sedimentation*, 544 pp., Prentice-Hall, Upper Saddle River, N. J.

Longuet-Higgins, M. S. (1950), A theory of the origin of microseisms, *Philos. Trans. R. Soc. London, Ser. A*, *243*, 1–35.

Meteorology International Inc. (1977), Deep water wave statistics for the California Coast, report, Sacramento, Calif.

Moore, L. J., and G. B. Griggs (2002), Long-term cliff retreat and erosion hotspots along the central shores of the Monterey Bay National Marine Sanctuary, *Mar. Geol.*, *181*, 265–283.

Nelson, R. C., and E. J. Leslighter (1985), Breaker height attenuation over platform coral reefs, in *1985 Australian Conference on Coastal and Ocean Engineering*, pp. 254–267, Brookfield Publ., Philadelphia, Penn.

Perg, L. A., R. S. Anderson, and R. C. Finkel (2001), Use of a new 10Be and 26Al inventory method to date marine terraces, Santa Cruz, California, USA, *Geology*, *29*, 879–882.

Ross, D. C. (1979), Description of and direction to selected Salinian block basement rock outcrops, Santa Lucia and Gabilan Ranges, California, *U.S. Geol. Surv. Open File Rep.*, *79-0383*.

Sanders, N. K. (1968), The development of Tasmanian shore platforms, report, Univ. of Tasmania, Hobart.

Stephenson, W. J., and R. M. Kirk (2000), Development of shore platforms on Kaikoura Peninsula, South Island, New Zealand, part I: The role of waves, *Geomorphology*, *32*, 21–41.

Sunamura, T. (1992), *Geomorphology of Rocky Coasts*, 302 pp., John Wiley, Hoboken, N. J.

Tillotson, K., and P. D. Komar (1997), The wave climate of the Pacific Northwest (Oregon and Washington): A comparison of data sources, *J. Coastal Res.*, *13*, 440–452.

Trenhaile, A. S. (1987), *The Geomorphology of Rock Coasts*, 384 pp., Clarendon, Oxford, U. K.

Weber, G. E. (1990), Late Pleistocene slip rates on the San Gregorio fault zone at Point Ano Nuevo, San Mateo County, California, in *Geology and Tectonics of Coastal California, San Francisco to Monterey (Volume and Guidebook)*, edited by R. Garrison, pp. 193–203, Pac. Sect. Am. Assoc. of Petrol. Geol., Bakersfield, Calif.

Weichert, E. (1904), Verhandlungen der Zweiten Internationalen Seismologischen Konferenz, in *Gerlands Beitrag Geophysik*, pp. 41–43, W. Englemann, Leipzig, Germany.

Zopf, D. O., H. C. Creech, and W. H. Quinn (1976), The wavemeter: A land-based system for measuring nearshore ocean waves, *Mar. Technol. Soc. J.*, *10*, 19–25.

P. N. Adams, Department of Earth Sciences, University of California, Santa Cruz, CA 95064, USA. (adamsp@es.ucsc.edu)

R. S. Anderson, Department of Geological Sciences, University of Colorado, Boulder, CO 80309-0450, USA. (andersrs@colorado.edu)

C. D. Storlazzi, U.S. Geological Survey, Pacific Science Center, Santa Cruz, CA 95060, USA. (cstorlazzi@usgs.gov)